Opto-Electronic
Advances

Supplementary information
July 2023, Vol. 6, No. 7

DOI: 10.29026/oea.2023.220073

All-optical controlled-NOT logic gate achieving directional asymmetric transmission based on metasurface doublet

Yijia Huang[1†], Tianxiao Xiao[2†], Shuai Chen[4], Zhengwei Xie[1], Jie Zheng[1], Jianqi Zhu[1], Yarong Su[1], Weidong Chen[1], Ke Liu[1], Mingjun Tang[1], Peter Müller-Buschbaum[2,3]* and Ling Li[1]*

[1]Laboratory of Micro-Nano Optics, College of Physics and Electronic Engineering, Sichuan Normal University, Chengdu 610101, China; [2]Physik-Department, Lehrstuhl für Funktionelle Materialien, Technische Universität München, James-Franck-Straße 1, 85748, Garching, Germany; [3]Heinz Maier-Leibnitz Zentrum (MLZ), Technische Universität München, Lichtenbergstraße. 1, 85748, Garching, Germany; [4]Tianjin Huahuixin Technology Group Co., Ltd, Zhongtian Avenue, Tianjin 300467, China.

†These authors contributed equally to this work.

*Correspondence: P Müller-Buschbaum, E-mail: muellerb@ph.tum.de; L Li, E-mail: lingli70@aliyun.com

This file includes:

Supplementary information for this paper is available at https://doi.org/10.29026/oea.2023.220073

Section 1: Conjugated directional performance for traditional metasurface

For traditional geometric phase-based metasurfaces, due to the reversed phase delay under opposite incident spins, these devices exhibit conjugated transmission performance[S1,S2]. As shown in Figure S1 as an example, the farfield response under LCP front incidence (RCP front incidence) is always equal to that under RCP back incidence (LCP back incidence).

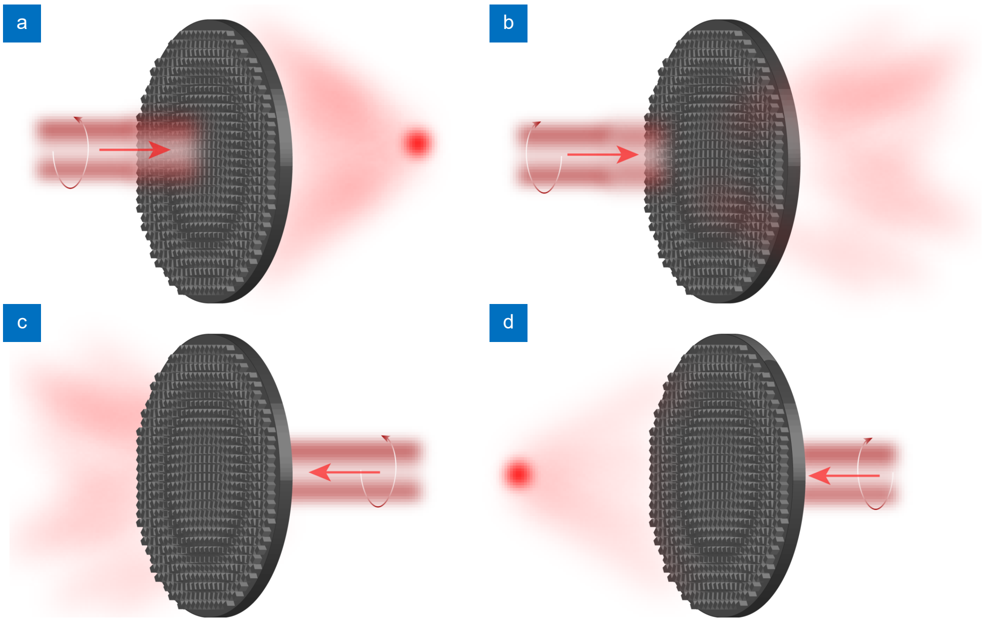

Fig. S1 | Far field responses under different incident conditions for traditional geometric phase-based metasurfaces. (**a**) RCP front incidence. (**b**) LCP front incidence. (**c**) RCP back incidence. (**d**) LCP back incidence.

Section 2: Transmission performance for HHWP and LHWP unit cells

To test the phase manipulation capability of LHWP and HHWP unit cells, full-wave simulations are performed for beam deflection. Considering the symmetry of the structure, periodic boundaries are employed in y-axis direction and open boundaries were used in x-axis and z-axis directions. The deflection angle is set as θ_t=15° and the corresponding phase distributions dΦ can be expressed as[S3]

$$\sin(\theta_t)n_t - \sin(\theta_i)n_i = \frac{\lambda}{2\pi}\frac{\mathrm{d}\Phi}{\mathrm{d}x}, \tag{S1}$$

where n_t=n_i=1 are the refractive index of air, θ_i=90° is the incident angle, λ is the working wavelength, dΦ/dx is the phase discontinuity. In our case, dx=P=4.5 μm. It can be inferred from Fig. S2(a) that nearly half of the incident light

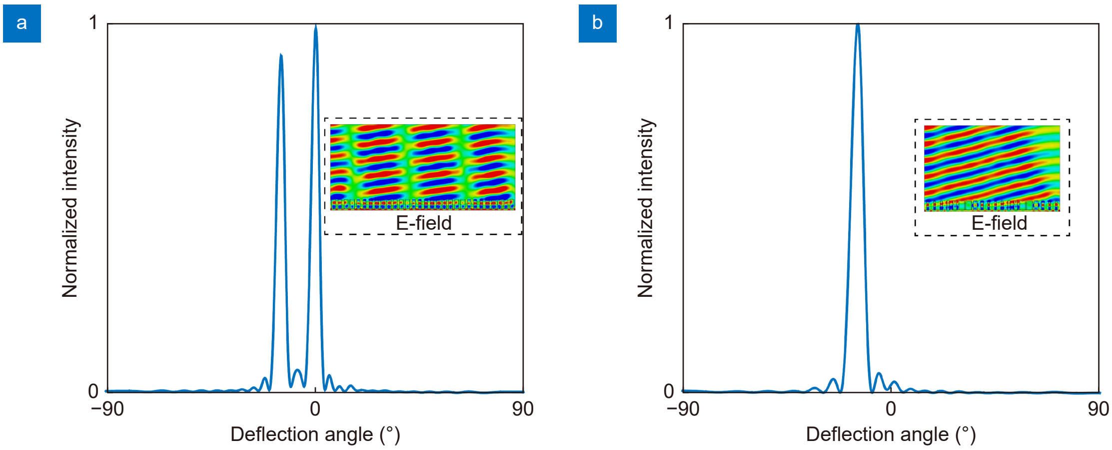

Fig. S2 | Deflection performance with metasurfaces composed of LHWP (**a**) and HHWP (**b**) unit cells at 28.3 THz. The insets show corresponding electric field distributions.

will be deflected to predesigned angle with LHWP unit cells, while nearly all the transmitted light will be deflected in Fig. S2(b) with HHWP unit cells.

Section 3: Detailed calculations based on geometric optics

According to geometric optics[S4], the focal distance F_3 of a doublet composed of a convex lens and a concave lens can be calculated by

$$\frac{1}{F_3}=\frac{1}{F_1}-\frac{1}{F_2}+\frac{d}{F_1F_2}\,, \tag{S2}$$

where F_1 and F_2 are the focal distances for convex lens and concave lens, respectively. d is the distance between two lenses. If d is much smaller than F_1 and F_2, the third term on the right side can be omitted and Eq. S2 can be simplified as that in the main text.

Section 4: Simulated results for the asymmetric metasurface doublet

To reduce the amount of calculation, cylindrical metalenses are simulated instead of spherical ones. The doublet diameter is d_2=900 μm with 20 unit cells on each side, focal distances f_1 and f_2 are 3d_2 and 9d_2, and the substrate thickness is set as 1 μm. Therefore, considering the symmetry of the structure, periodic boundaries are employed in y-axis direction and open boundaries are used in x-axis and z-axis directions. The simulated far field results under different incident conditions are shown in Fig. S3. Since the focusing intensity for cylindrical lens is intrinsically much lower than same-sized spherical lens and the metasurface doublet is with wavelength scale, the simulated ICR is unavoidably decreased. However, the simulated results still match well with their calculated counterparts in Fig. 3 that four different outputs can be clearly observed.

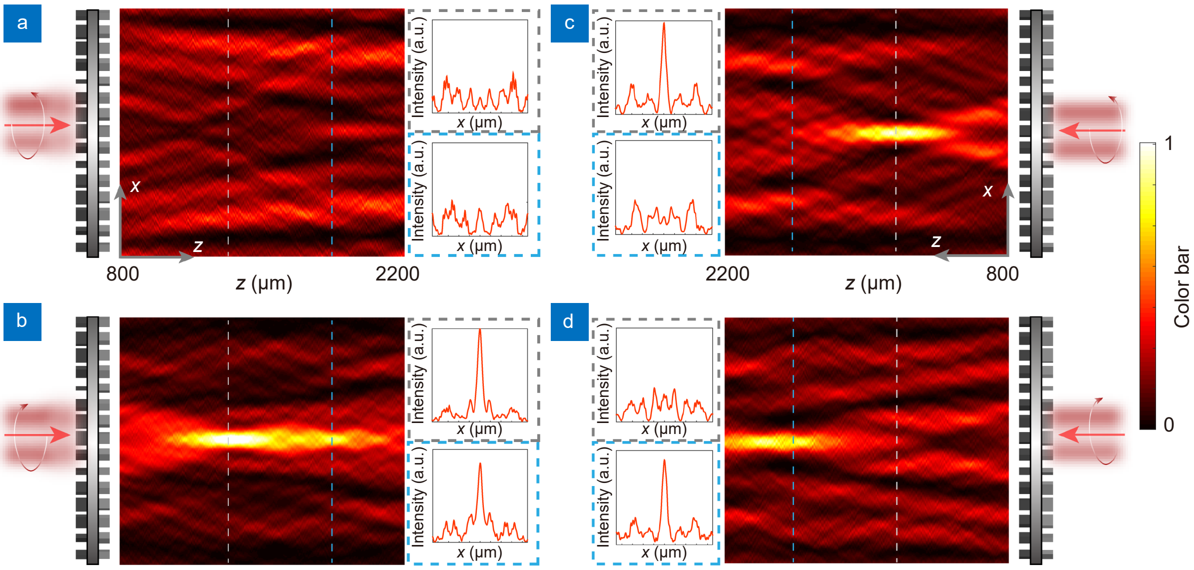

Fig. S3 | Simulated farfield results in *x-z* plane under different incident conditions. (**a**) Front RCP incidence. (**b**) Front LCP incidence. (**c**) Back RCP incidence. (**d**) Back LCP incidence. The insets show the 1D normalized intensity distributions at z=18 mm (white dashed lines) and 27 mm (blue dashed lines)

Section 5: The measured optical path for the all-optical CNOT LG

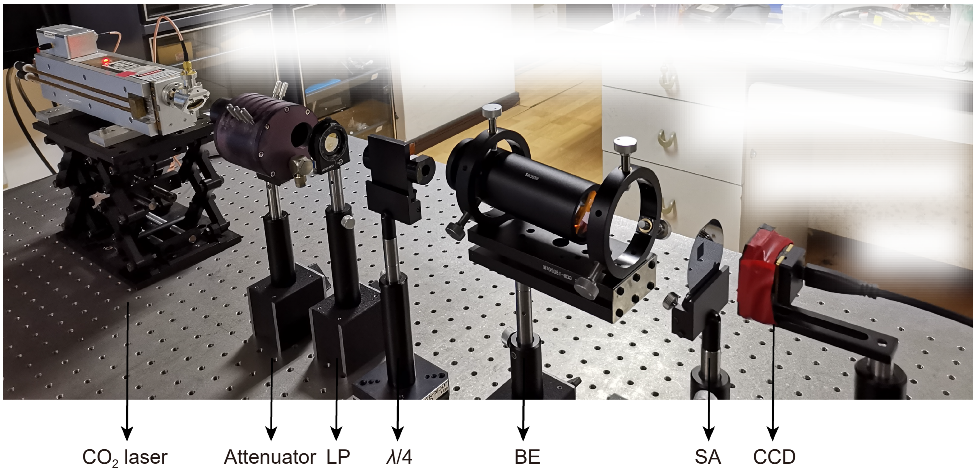

Fig. S4 | Optical path of the measurement setup. LP: linear polarizer. λ/4: quarter wave plate. BE: beam expander. SA: sample.

Section 6: Cross section views on the focal plane

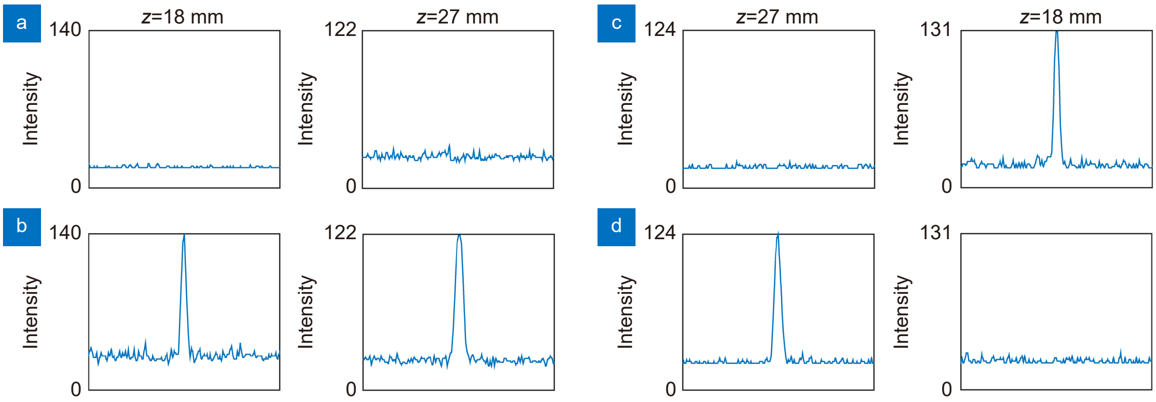

Fig. S5 | Cross section views on the focal plane. (**a**–**d**) correspond to the results in Fig. 4(c–f), respectively.

Section 7: Simulated results in a certain bandwidth

Due to the wavelength-independent nature of geometric phase as well as the simulated response of the unit cells, the proposed device in Fig. 3 can work efficiently in a certain bandwidth. Figure S7 depicts the farfield results under different incident conditions at 27 and 29 THz. Obviously, the results are similar to that in Fig. 3 except for slight shift of focal distances. The deviations can be attributed to different phase accumulations in free space at various frequencies.

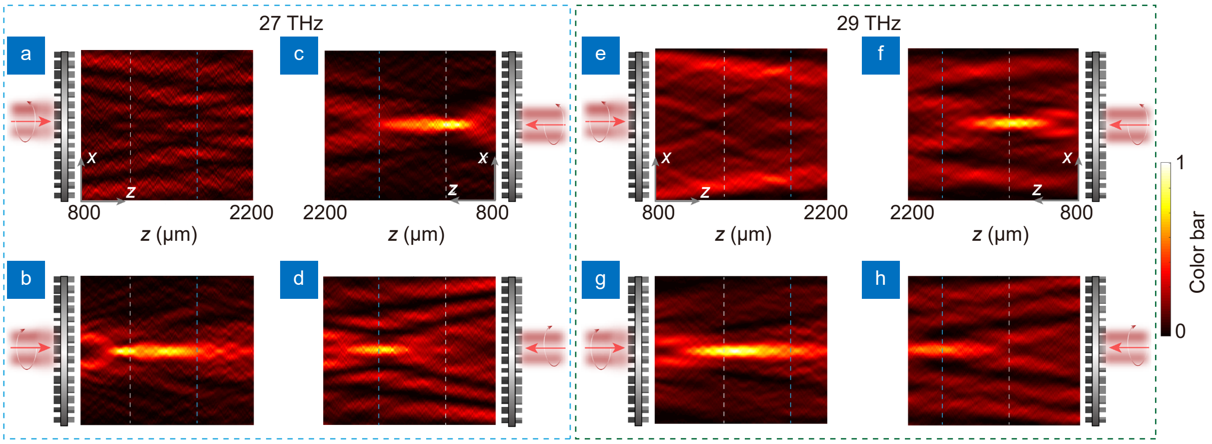

Fig. S6 | Farfield results for the proposed device under different incident conditions at different frequencies. (**a**–**d**) Farfield results at 27 THz. (**e**–**h**) Farfield results at 29 THz. The definitions are the same as those in Fig. 3.

Section 8: Shaping the focal spot with extra phase modulations

Since the working mechanism of the proposed all-optical CNOT LG is based on focusing effect, the focal spot in the farfield can be easily shaped when extra phases are added. As an example, Fig. S6 depicts the farfield responses under different incident conditions at 28.3 THz when a vortex phase $\Phi=l\theta$ is added to M2 while other settings are the same as that in Fig. 3, where $l=2$ is the topological charge and θ is the azimuthal angle[S5]. In this case, the focal spot at $z=f_3$ is a focused vortex beam with donut shaped. The focal spot can be further altered when changing the value of l or adding other more complex phase distributions, which will enable more applications for the proposed device.

Section 9: Schematic diagram of the fabrication process

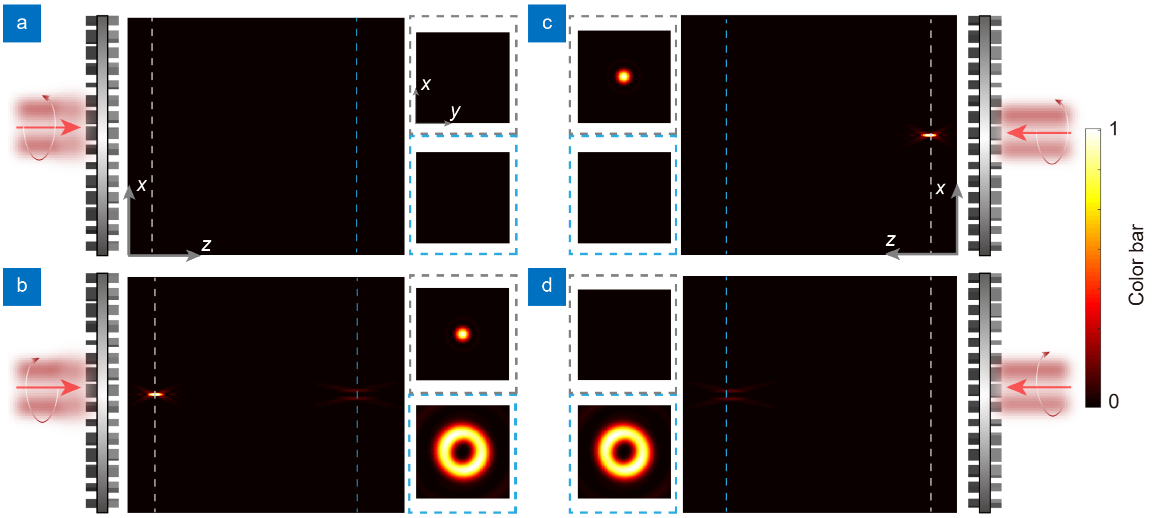

Fig. S7 | Numerical farfield results in *x-z* plane under different incident conditions when adding a vortex phase to M2. (**a**) Front RCP incidence. (**b**) Front LCP incidence. (**c**) Back RCP incidence. (**d**) Back LCP incidence. The insets show the 2D normalized intensity distributions at *z*=18 mm (white dashed lines) and 27 mm (blue dashed lines).

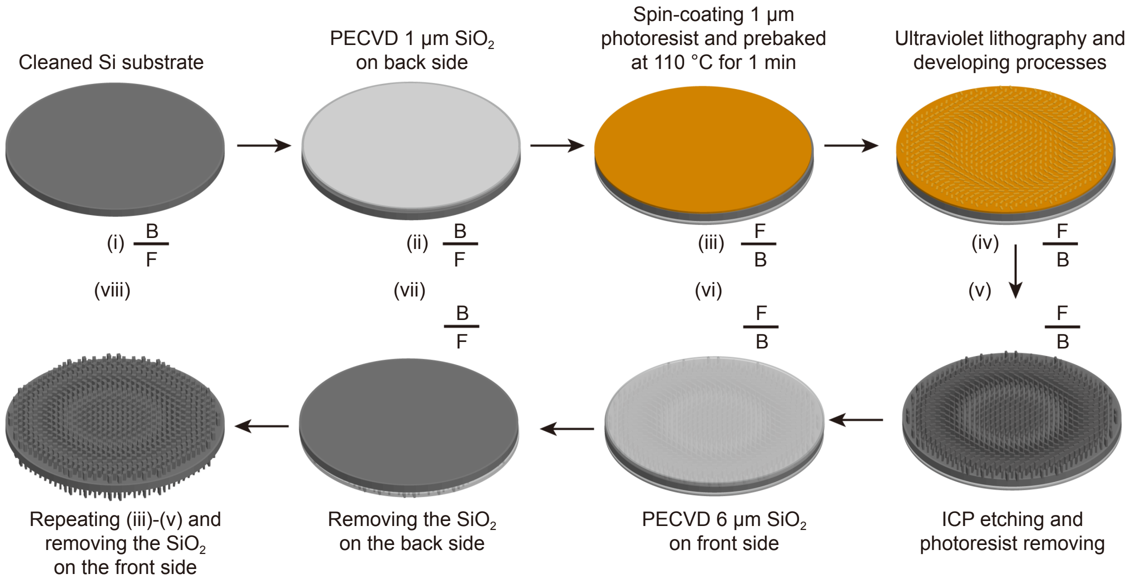

Fig. S8 | Schematic diagram of the fabrication process. The proposed devices are mainly fabricated by the ultraviolet lithography and ICP etching processes. F: front side. B: back side.

Section 10: Influence of the fabrication imperfection on the performance of the device

Since the polarization conversion rations for the fabricated HHWP and LHWP unit cells may deviate from their simulated counterparts due to fabrication imperfection, this section will discuss the corresponding influence. As the proposed metasurface doublet contains two kinds of unit cells on each side of the substrate, we discuss this issue separately.

On the one hand, if the proposed LHPW unit cells cannot achieve the performance as shown in Fig. 2(g), for example, the cross-polarized component is much lower than its co-polarized counterpart, then the intensity distribution for the focal spots in Fig. 3 and Fig. 4 will be altered. Specifically, in this case, the intensity for the focal spot at $z=f_1$ will increase and that at $z= f_3$ will decrease. On contrary, when the co-polarized component is much lower than its cross-polarized counterpart for the LHPW unit cells, the intensity for the focal spot at $z= f_1$ will decrease and that at $z= f_3$ will increase. In fact, the mentioned results can be easily obtained from geometric optics. It should be mentioned that the deviation of polarization conversion rations of LHWP unit cells will only influence the intensity of the focal spots but the asymmetric transmission performance still exists.

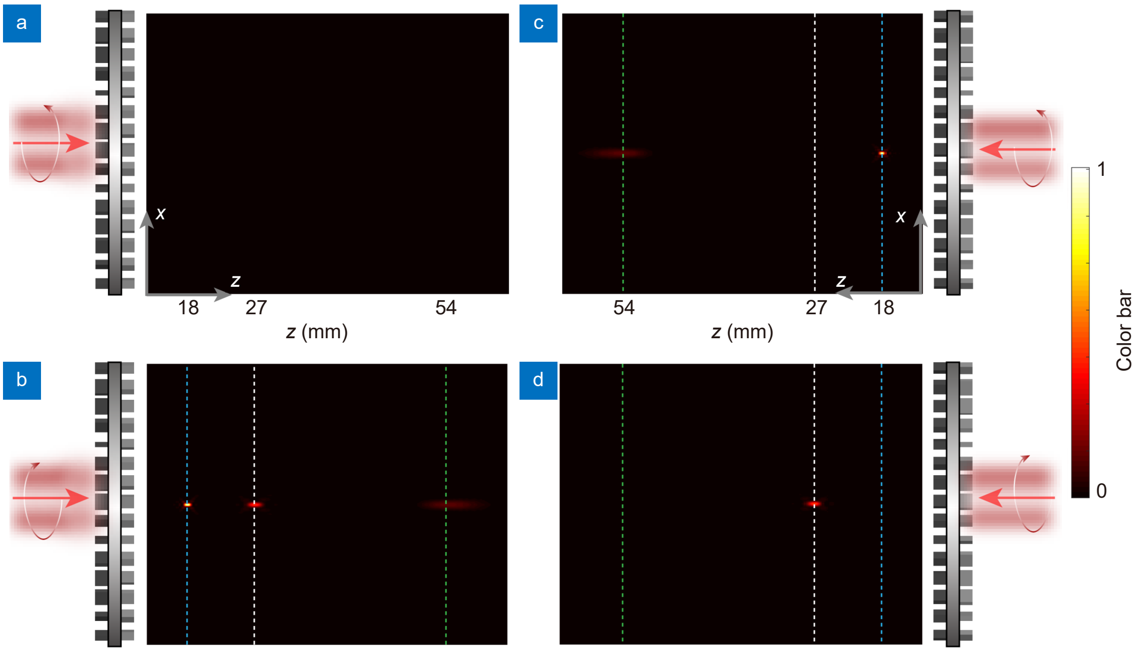

Fig. S9 | Numerical farfield results in *x-z* plane under different incident conditions when the HHWP unit cells on the front side in Fig. 3 changed to LHWP unit cells. (**a**) Front RCP incidence. (**b**) Front LCP incidence. (**c**) Back RCP incidence. (**d**) Back LCP incidence. The blue, white and green dotted lines indicate $z=f_1$, f_3 and f_2, respectively.

On the other hand, if the proposed HHPW unit cells cannot achieve the performance as shown in Fig. 2(c), for example, if the doublet is composed of two layers of LHPW unit cells, the theoretical results are shown in Fig. S9. It can be inferred from Fig. S9 that except for the focal spots at $z= f_1$ and $z= f_3$, there is another focal spot at $z= f_2$ as shown in Fig. S9(b) and S9(c). However, one can still observe the asymmetric transmission performance in this case.

Besides, since the focal distance for $z= f_2$ is much larger than other two cases, the field intensity is intrinsically weak compared with other two cases. In fact, when the cross polarized component is slightly larger than the co-polarized component, the field intensity at $z= f_1$ and $z= f_3$ will be much larger than that at $z= f_2$. For example, Figure S10 shows the numerical farfield results in *x-z* plane under different incident conditions when the cross polarized component is four times larger than the co-polarized component. As shown in Figure S10(b), the field intensity I_{f1}: I_{f2}: I_{f3}=34:1:15. In this case, the farfield distributions are nearly the same as those in Figure 3 that the focal spot at $z= f_2$ can hardly be observed.

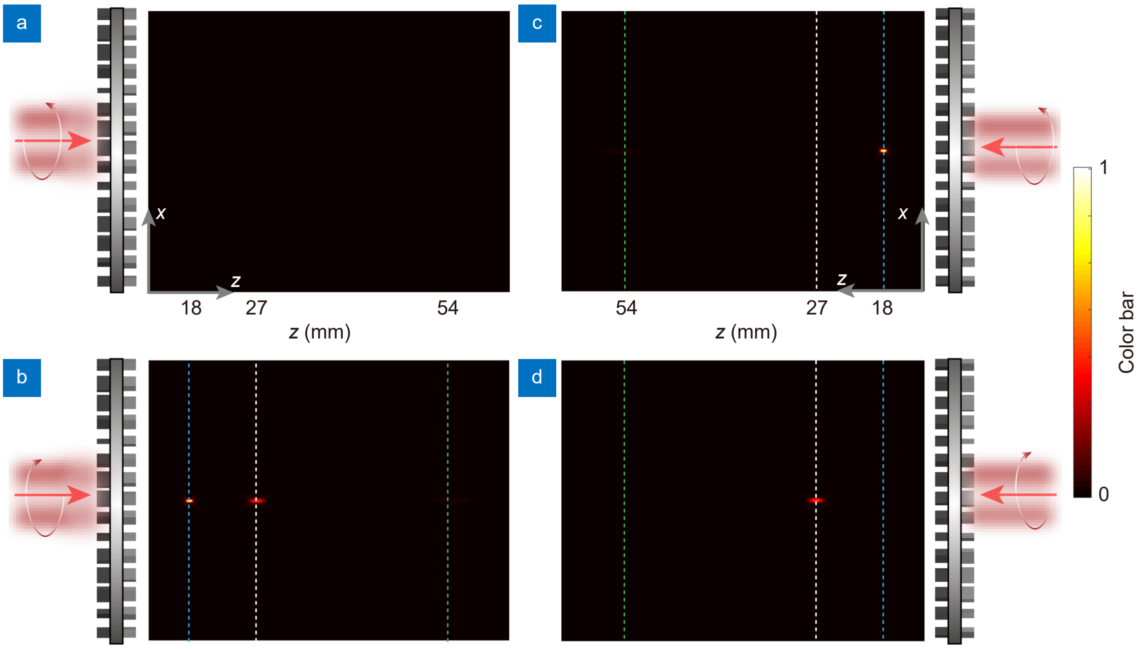

Fig. S10 | Numerical farfield results in *x*-*z* plane under different incident conditions when the cross polarized conversion ratio is four times larger than the co-polarized component. (**a**) Front RCP incidence. (**b**) Front LCP incidence. (**c**) Back RCP incidence. (**d**) Back LCP incidence. The blue, white and green dotted lines indicate $z=f_1$, f_3 and f_2, respectively. In this case, the focal spot at $z= f_2$ can hardly be observed.

Table S1 | comparison between the proposed device and other previously reported works.

Reference in the main text	Type	Precise manipulation of light	Detecting method	Experiment
ref.[6]	Nonlinear	Yes Precise control of the incident energy	Near-field	Yes
ref.[8]	Nonlinear	Yes Precise control of the control pulse and the probe light	Near-field	Yes
ref.[9]	Linear	Yes Precise control of the incident location and phase difference	Near-field	Yes
ref.[10]	Linear	Yes Precise control of the incident location	Near-field	Yes
ref.[11]	Linear	Yes Precise control of the incident location	Near-field	No
ref.[12]	Linear	Yes Precise control of interference conditional	Far-field	Yes
ref.[41]	Linear	Yes Precise control of interference conditional	Far-field	No
ref.[42]	Linear	No	Far-field	No
ref.[43]	Linear	Yes Precise control of the incident location	Far-field	Yes
This work	Linear	No	Far-field	Yes

References

S1. Bliokh KY, Rodríguez-Fortuño FJ, Nori F, Zayats AV. Spin–orbit interactions of light. *Nat Photonics* **9**, 796–808 (2015).

S2. Cardano F, Marrucci L. Spin–orbit photonics. *Nat Photonics* **9**, 776–778 (2015).

S3. Yu NF, Genevet P, Kats MA, Aieta F, Tetienne JP et al. Light propagation with phase discontinuities: generalized laws of reflection and refraction. *Science* **334**, 333–337 (2011).

S4. Mansuripur M. *Classical Optics and its Applications* (Cambridge University Press, Cambridge, 2002).

S5. Jin JJ, Pu MB, Wang YQ, Li X, Ma XL et al. Multi-channel vortex beam generation by simultaneous amplitude and phase modulation with two-dimensional metamaterial. *Adv Mater Technol* **2**, 1600201 (2017).

S6. Georgi P, Wei QS, Sain B, Schlickriede C, Wang YT et al. Optical secret sharing with cascaded metasurface holography. *Sci Adv* **7**, eabf9718 (2021).